*Painting by Vincent Van Gogh in 1889 [13], image from [14] Notes: see ***

Introduction into the statistics of turbulent flows

University of Glasgow

Nicholas Cheong

Dr Angela Busse

**Vincent Van Gogh's paintings typically convey a sense of dynamical movement with his use of variant luminosity throughout each painting. For his *Starry Night* painting, the dynamical movement is synonymous to turbulence in which was first discovered when compared with an image from the NASA/ESA Hubble space telescope, where the eddies are formed in the dust and gas surrounding the stars and highlighted by the starlight. The probability density function (PDF) was established with the luminance fluctuations of the painting and compared with that of velocity fluctuations of a turbulent flow; the results compared well and his use of variant luminosity exhibit features akin to turbulent structures [1].

Contents

Nomenclature

δ	Half-channel height
x, y, z	Spatial positions in the streamwise, wall normal and spanwise direction
y_+	Non-dimensional wall distance
τ_w	Wall shear stress
ρ	Fluid density
Re_τ	Reynolds shear number
Re	Reynolds number
d	Dice number
$\bar{d}$	Random variable dice number
N	Number of occurrences
p	Probability
$P(U)$	Probability function
u	Streamwise velocity
v	Wall-normal-wise velocity
U	Streamwise mean velocity
u_{bulk}	Bulk velocity
δ_v	Viscous length scale
H	Channel height
k	Turbulent kinetic energy
$\overline{uv}$	Reynolds stresses
ω	Specific dissipation of turbulent kinetic energy
ϵ	Dissipation of turbulent kinetic energy

Overview of turbulence

Turbulence is a phenomenon in fluid dynamics which has been widely studied to unlock more efficient and accurate models in which are required to simulate the effects of turbulence. Turbulence affects a wide variety of engineering quantities such as aerodynamic and hydrodynamic forces, heat transfer and mixing [2] and therefore the accuracy of turbulence modelling is imperative for design and analysis. The understanding of the chaotic nature of turbulence has provided a challenge for engineers, physicists and mathematicians alike [3] and this assignment will, so to speak, scratch the surface of the work that has been achieved over the past decades.

Turbulence motion has two key characteristic features which are the dissipation of kinetic energy and its mixing ability. Within a turbulent flow, the fluid elements move in multiple directions in which therein lies its mixing ability. For the dissipation of kinetic energy, the flow has a variant size, or scales, of eddies and the dissipation of kinetic energy is where the larger eddies disperse into smaller eddies, which in turn, disperse into even smaller eddies and the smallest eddies are completely dissipated by viscous effects. This is commonly known as the energy cascade [3]. Since the nature of turbulence is chaotic, statistical descriptions such as the mean, variance and skewness [3] are necessary to obtain meaningful properties of the flow which can be interpreted and implemented to a problem under analysis. Turbulent flows can be statistically categorized into two types, homogenous and non-homogenous [3].

The former definition in the spatial dimensions is where the flow is not dependent on the position of the flow. This is the flow being fully developed in the direction of homogeneity. In terms of the time dimension, homogeneous in time is commonly referred to as stationary [3], which is so named as the flow will appear stationary if it does not vary in time. Furthermore, if the flow is fully developed in two out of three spatial dimensions, the benefits of homogenous flow allows the dimension which varies to be isolated from the other two, therefore, allowing the stochastic nature of the turbulent system to be interpreted easier. There are two subclasses of homogenous statistical descriptions, isotropic and anisotropic. Isotropic is where the flow exhibits properties of statistical symmetry, in which is useful for analysis and is where the statistical properties show no directional preference. Anisotropic is the opposite of isotropic, in which, the flow velocity has a directional dependence [2], [3].

The non-homogenous statistical description is where the statistical quantities are a function of position; examples of this are typically turbulent boundary layers and channel flow on the wall-normal coordinates [2].

Chapter 1

Analysis of velocity data for fully developed channel flow

1.1 Objectives and Overview

The objective of this assignment was to gain insight into the effects of near wall turbulence on the velocity profile of a flow. This analysis was executed in a channel to simulate standard channel flow which characteristics are widely known and therefore useful to explore for an understanding of turbulent flow.

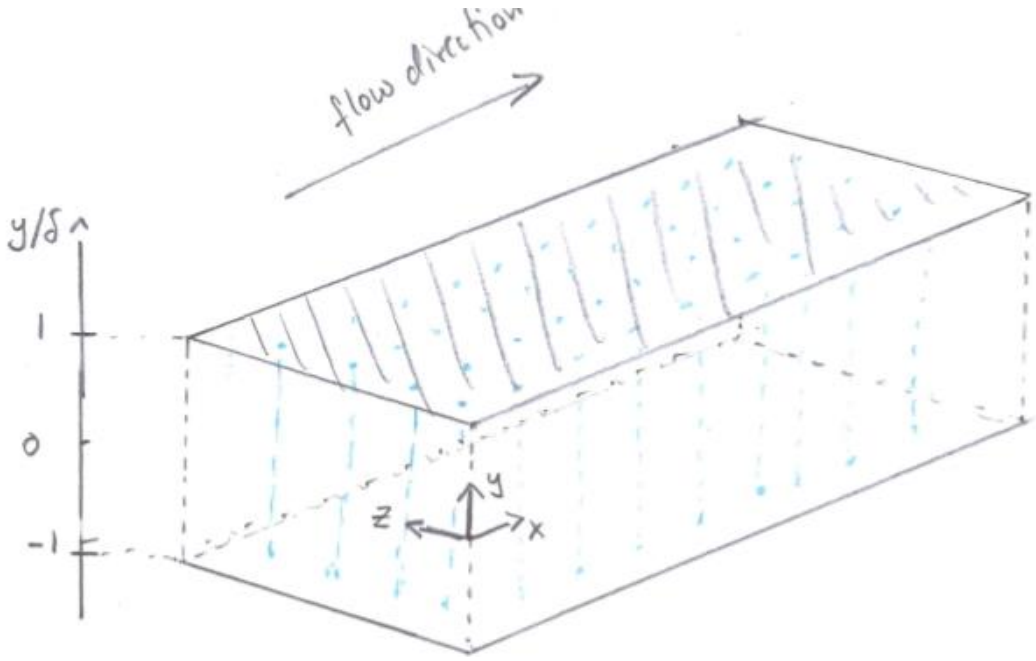

Figure 1.1 - Fluid domain, image courtesy of Dr Angela Busse

For the flow domain under analysis, x, y and z are synonymous to the streamwise, wall normal and spanwise directions, where the wall normal coordinates are normalised by the half-channel height, δ. The data for the velocity profiles was obtained from Direct Numerical simulations (DNS) where the Navier Stokes equations are solved directly and provides the highest degree of accuracy when simulating fluids, however, with the downfall of being the most computationally expensive method. The flow is subjected to a constant mean streamwise

pressure gradient which drives the flow in the streamwise direction. It was also considered fully developed in the streamwise and spanwise directions (homogenous) which was attained with the use of periodic boundary conditions on the respective directions. Full development in two out of the three directions is useful for analysing turbulent velocity profiles as it removes the flow dependency of the fully developed directions and therefore allows the remaining non-homogenous direction to be analysed in an isolated condition, in which, for this case is the wall-normal direction. Furthermore, the flow is also considered statistically symmetrical around the centreline $y/\delta = 0$ and the wall-normal distances for the numerical analysis were set such that the distances were smaller at the near-wall region, likely to give a y_+ value of 1 to place the first near-all cell in this viscous sublayer. The velocity data was taken over 20 time units and normalized by δ/u_τ, where u_τ is the shear velocity which equates to the square root of the shear stress over density as denoted in equation 1. All velocity components were also normalized by the shear velocity, this is known as the non-dimensional variable, u_+.

$$u_\tau = \sqrt{\frac{\tau_w}{\rho}} \qquad (1)$$

The Reynolds shear number, Re_τ, is 180 for this experiment. This is over the limits of $Re_\tau >$ 100 which means that the turbulence within the flow will be sustained [3].

1.2 Investigating the turbulent velocity profile

The data was extracted in multi-paradigm numerical software, Matlab, and was processed in various methods to explore the characteristics of the profile.

1.2.1 Velocity variations in time

The velocity data was plotted against time for different wall normal locations to investigate the effects of the relative distance to the wall on the velocity fluctuations. The wall distances were $y/\delta = -0.9981, -0.9226$ and -0.6942 where the wall coordinate in the wall-normal direction of -1. This corresponds to $yloc$ indices of 35, 15 and 1 respectively and is highlighted in figure 1.1 in which entails a plot of the wall-normal grid lines in the mesh used to simulate the flow. Furthermore, the effects of the streamwise and spanwise location was also considered to highlight the flow is statistically homogenous (fully developed).

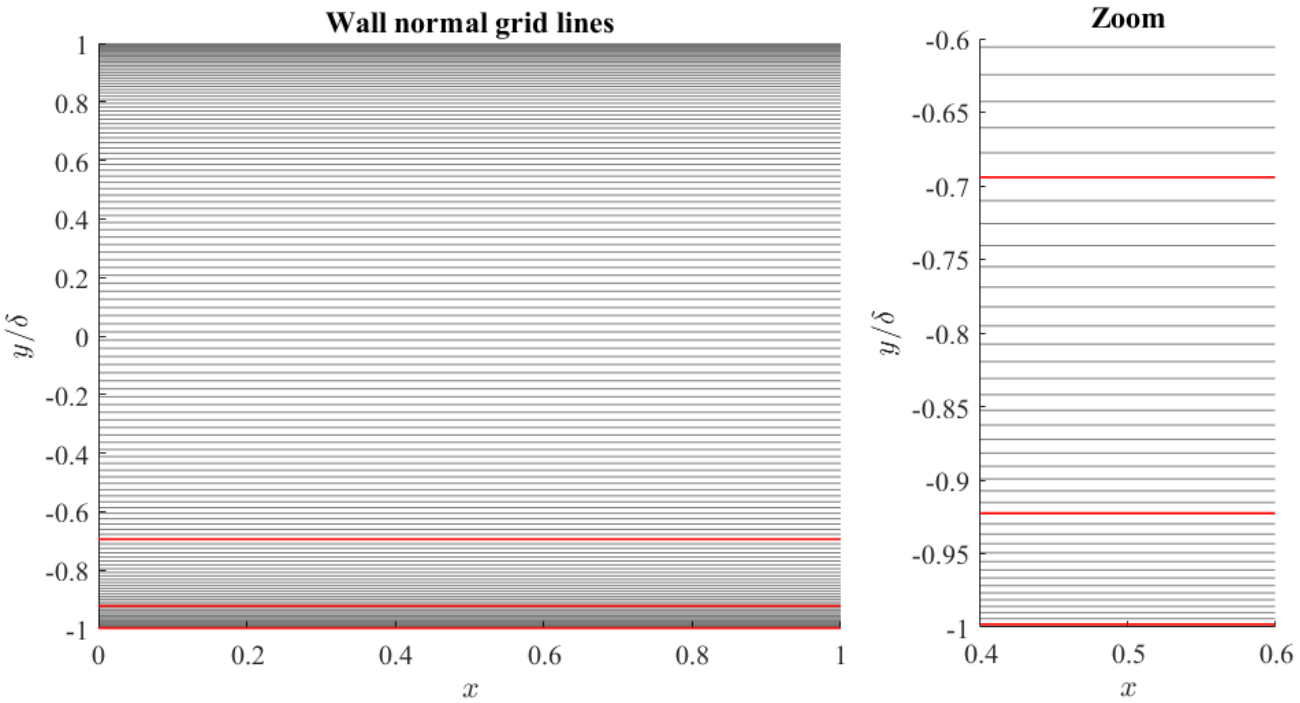

Figure 2.2 - Wall normal grid lines, where the red lines indicate the locations under analysis. To the right, a close-up of the locations for clarity. Note, x is quantified, however, since periodic boundaries are applied this quantity is arbitrary.

The velocity variation with time is depicted for each wall-normal location in figures 1.3, 1.4 and 1.5. The erratic behaviour of the velocity clearly highlights the stochastic nature of turbulence.

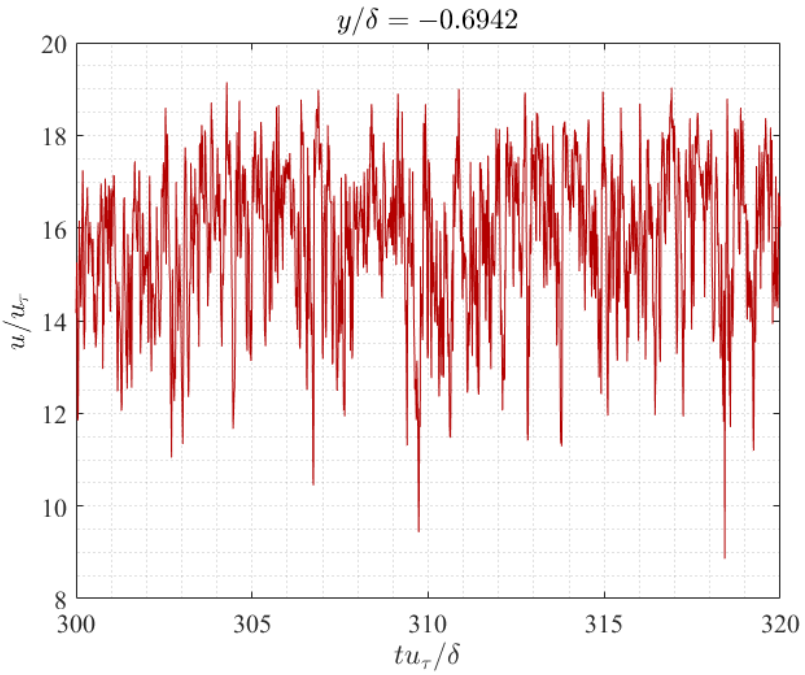

Figure 1.3 – Velocity against time for a wall normal position of $y/\delta = -0.6942$

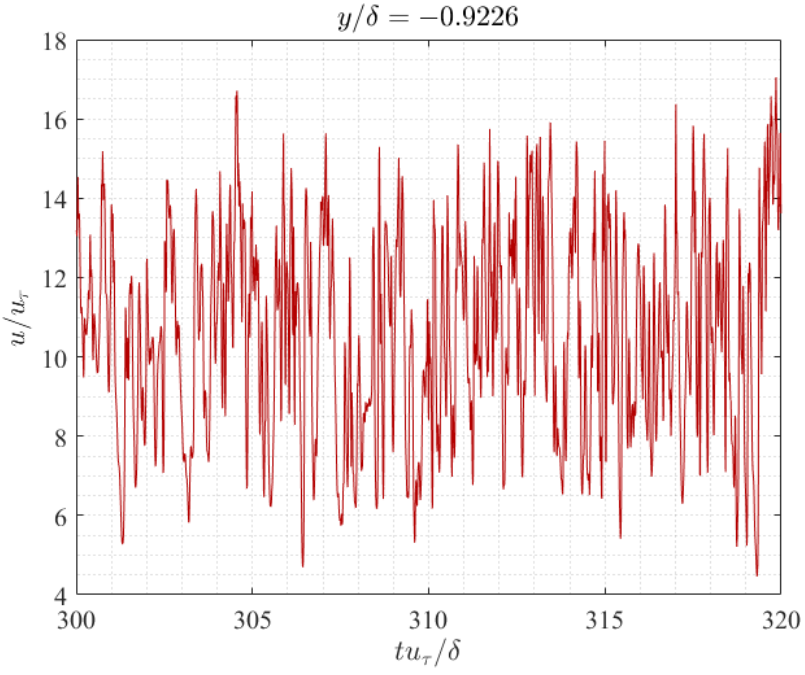

Figure 1.4 – Velocity against time for a wall normal position of $y/\delta = -0.9226$

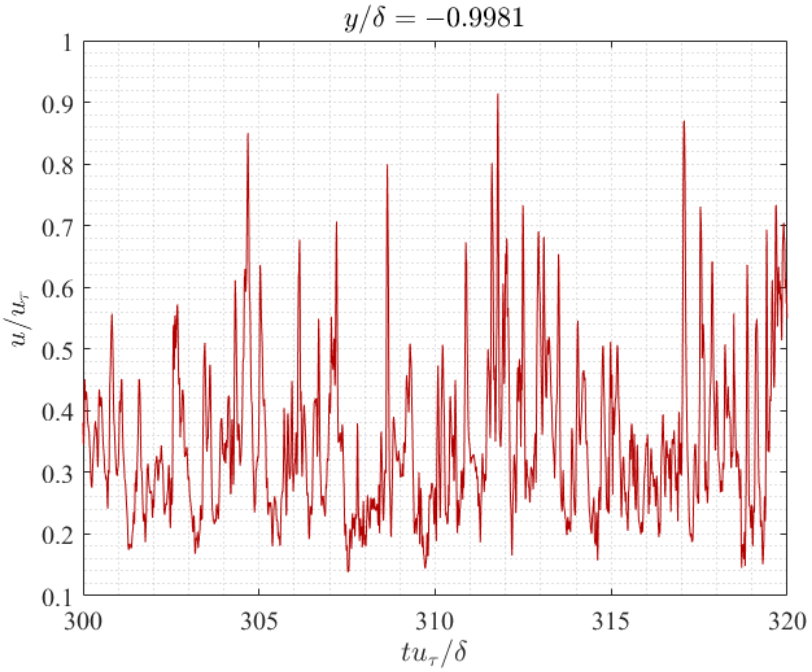

Figure 1.5 - Velocity against time for a wall normal position of $y/\delta = -0.9981$

Notably, the mean velocities are dependent on the wall-normal location where the velocity decreases as the wall-normal location approaches the wall. This is of course due to the near-wall viscous effects reducing the kinetic energy and therefore the overall mean flow speed [3]. Furthermore, each velocity-time signal is erratic due to the velocity fluctuations; however, it is less erratic the closer to the wall due to the dissipation of kinetic energy, which is evident in figure 1.3 where the lower side velocity peaks, or fluctuations, are closer to the mean value.

The velocity variation at different spanwise and streamwise locations are displayed in figure 1.6:

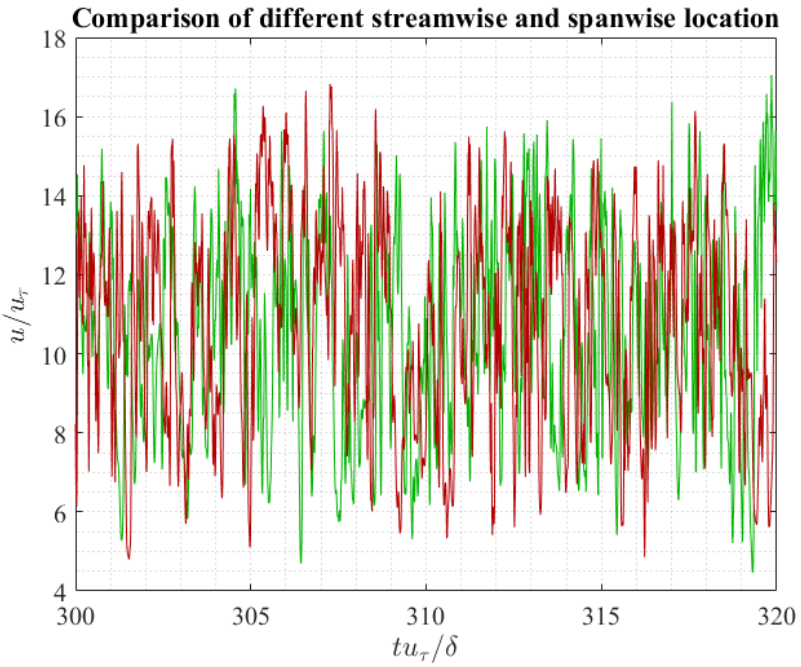

Figure 1.6 – Comparison of velocity with time signals of different streamwise and spanwise positions at $y/\delta = -0.9226$

From this, the clear characteristics are that the mean velocity is similar which is due to the flow being statistically homogenous in the spanwise and streamwise direction. However, slight differences may arise due to the limited quantity of timesteps used, therefore, not being considered to have full statistical convergence.

1.2.2 Statistics of the turbulent flow

Probability is an important statistic to turbulent flow and is determined from the number of occurrences of a value in relation to the total number occurrences. For example, the roll of a dice is a deterministic system with possible values ranging from $1 \rightarrow 6$, the probability of the dice rolling on 3 is [3]:

$$\bar{d} = \sum_{j=1} \frac{N_{j=3}}{N} d_{j=3} \tag{2}$$

Where $\bar{d}$ is the random variable dice roll, N the total number of rolls, $N_{j=3}$ the number of rolls which resulted in the occurrence of 3, and $d_{j=3}$ is the number under analysis [3]. The probability of the dice rolling on 3 results as:

$$p_{j=3} = \frac{N_{j=3}}{N} \tag{4}$$

Note, the above is for a deterministic system as mentioned, however, for a continuous system where the values can range infinitely between limits, the integral is required [3]. This continuous system can typically be turbulence, where the values of velocity of a velocity time signal can be any value between the set limits of the erratic nature. Changing the notation of $d \rightarrow u$ to denote velocity:

$$\bar{u} = \int_{u_{lower}}^{u_{upper}} u_{value} P(u_{value}) du \tag{5}$$

Where $P(u_{value})$ is the probability density function which describes the distribution of the occurrences between the limits. Consider figure 1.7 which is the velocity-time signal at the wall normal location, $y/\delta = -0.9981$ and the upper and lower limits have been marked by the horizontal lines.

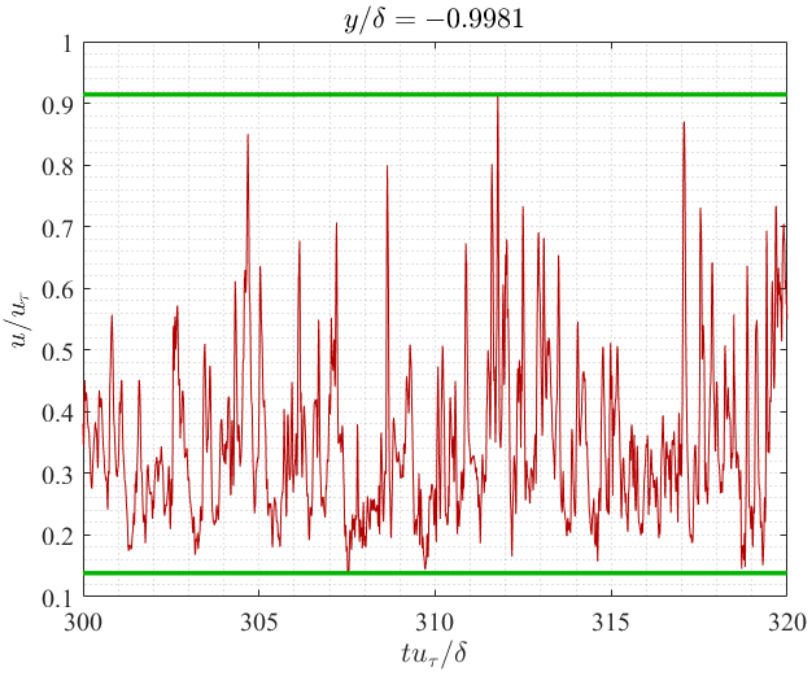

Figure 1.7 – Velocity-time signal at wall normal location -0.9981 with limits of maximum and minimum velocity magnitude denoted by green lines.

The probability density function will be between limits denoted by the green lines. Now, figure 1.8 and 1.9 denote the probability density function for different number of bins, 50 and 200 respectively, where the continuous data between the limits is categorized. Bins have an assigned value which is dependent on the number of bins and the limits.

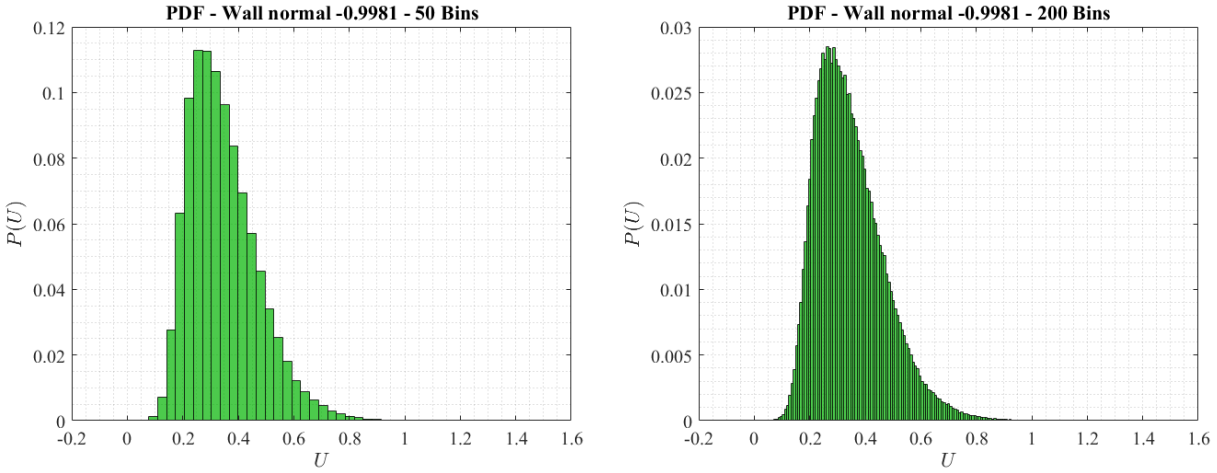

Figure 1.8 and 1.9 – PDF of wall normal location, $y/\delta = -0.9981$, with different bin sizes of 50 to 200.

From histogram plots, the bins do not fall below or above the limitations of the velocity-time signal and categorize each value of u depending on its value; the number of occurrences denote the probability and hence the height of each bin. The number of bins is important as it dictates how finely categorized the data is, further, the probability of each bin reduces as bin number increases as there is a finite number of data points to be distributed between bins.

Figures 1.10 denotes the PDF for wall normal locations $y/\delta = -0.9226$ and -0.6942 and table 1.1 displays the statistical properties of each.

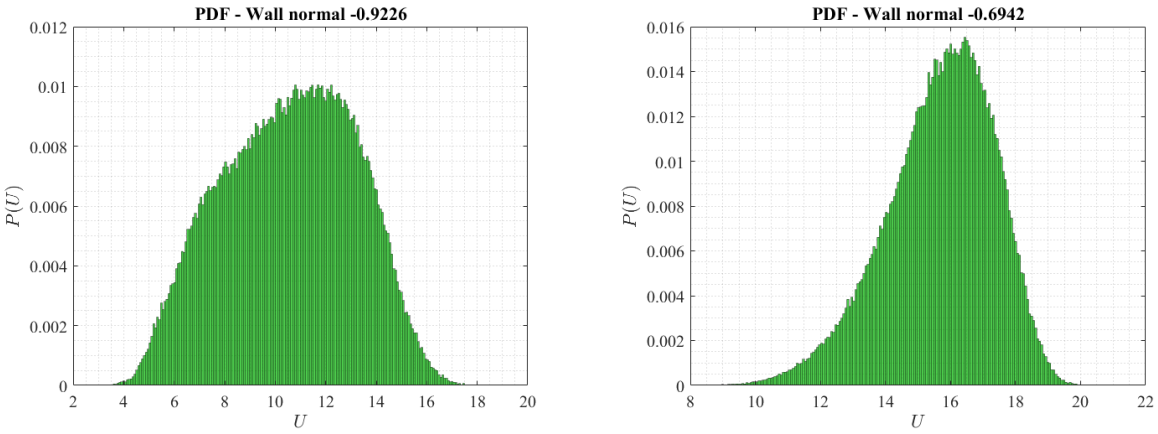

Figure 1.10 – PDF plots for $y/\delta = -0.9226$ (left) and -0.6942 (right)

Table 1.1 – Statistical properties of $y/\delta = -0.9226$ and -0.6942

$yloc$	y/δ	Skewness	Mean	Variance	Kurtosis
35	-0.9226	-0.522	15.67	2.764	3.123
15	-0.6942	-0.114	10.56	6.872	2.238

Firstly, the flow closer to the wall is slower due to the near-wall viscous effects which is evident in the overall mean values of the velocity-time signals.

The skewness of the signals is the measure of dissymmetry around the mean value of the data-set; in the case of the above, the skewness is negative where the velocity fluctuations occur less towards the wall which is evident in figure 1.10. However, the skewness increases as the wall-normal location becomes closer to the wall and eventually becomes positively skewed, such as

figure 1.9 which is in the near wall region. If no skewness occurs, the plot will form a typical Gaussian distribution [4],

The variance is also known as the root mean square [4] and measures the average deviation of each data set value with the mean. The variance increases closer to the wall due to the increase of shear the fluid is exerted to due to the steeper velocity gradients.

The kurtosis is the measure of the absolute gradient, or degree of flatness, of the PDF. A lesser degree of flatness in a PDF indicates that the velocity-time signal is significantly distributed between the limits. This is synonymous to more erratic behaviour which is known to occur in the near wall region, hence, the kurtosis increases the closer it becomes to the wall and approaches the buffer layer. However, the kurtosis decreases very close to the wall as the viscous effects begin to dominate, and the decreases in flatness can be seen by comparing figures 1.9 and 1.10.

PDF plots can also be created in two-dimensions, figure 1.11 displays the PDF for wall normal location, $y/\delta = -0.6942$, dependent on the streamwise and wall-normal respective velocities:

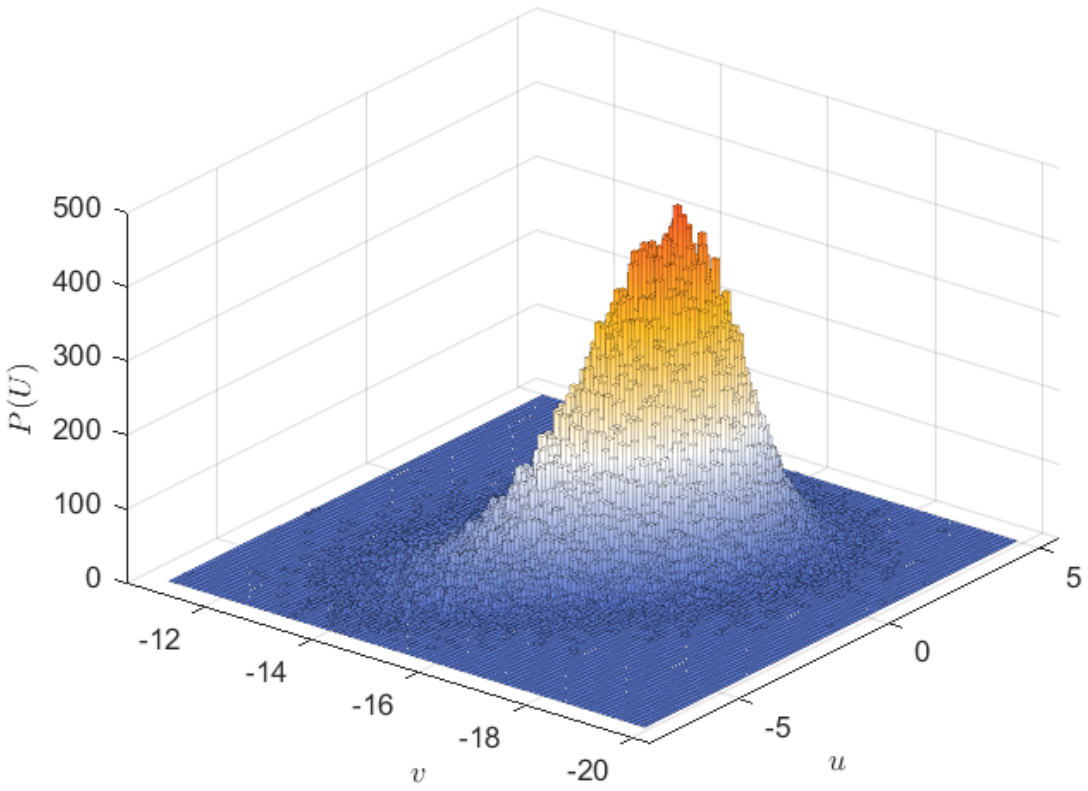

Figure 1.11 – PDF for two-dimensions in streamwise and wall normal location with 100 bins on each spatial dimension.

Notably, the probability function significantly increases which is due to the dependency on multiple dimension values. Plotting the PDF in two dimensions would be useful for non-spatial homogeneous flows in two-dimensions as it allows the user to visualize the statistical characteristics in both non-homogenous directions.

1.2.3 Instantaneous velocity profiles

Instantaneous turbulent velocity profiles are where the velocity profile is taken at a given time step. Figure 1.12 Display the profiles over different time units of $\frac{1}{100}\frac{u_\tau}{\delta}$, $5\frac{u_\tau}{\delta}$, $10\frac{u_\tau}{\delta}$, and $15\frac{u_\tau}{\delta}$, where the legend indicates the indices of the time units, where 1 time unit is equivalent to 100 indices.

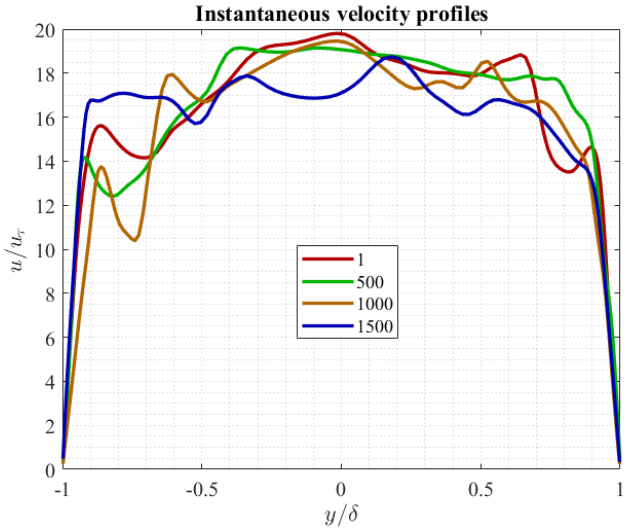

Figure 1.12 – Instantaneous turbulent velocity profiles for different time-units.

The velocity profiles follow roughly the same values over the time units which indicates statistical stationarity; the mean values of each profiles are similar.

1.2.4 Turbulent and laminar mean streamwise velocity profile

Figure 1.13 below indicates the difference between the averaged turbulent and laminar velocity profile where the mean velocity is $\frac{U}{u_\tau}$.

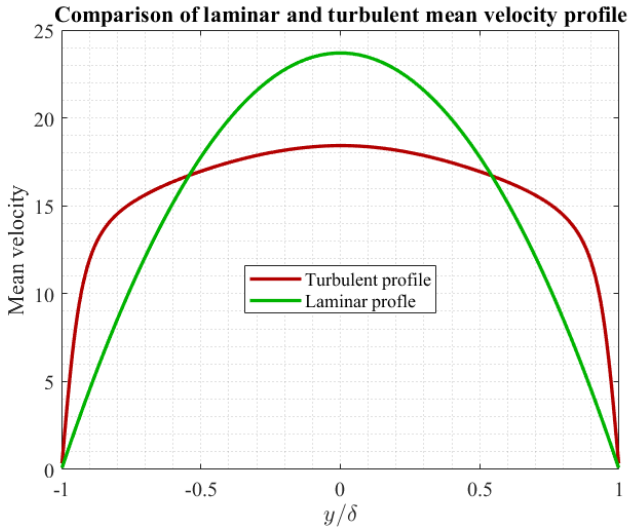

Figure 1.13 – Comparison of mean laminar and turbulent velocity profiles

The turbulent profile was averaged by taking the mean value of each velocity component. The laminar profile was calculated by finding the bulk velocity, and implementing it into equation 6:

$$U = 1.5u_{bulk}\left(1 - \left(\frac{y}{\delta}\right)^2\right) \tag{6}$$

$$u_{bulk} = \int_{-1}^{1} U\, d\left(\frac{y}{\delta}\right) \tag{7}$$

The clear difference between the velocity profiles is the velocity magnitude in the near-wall region. The higher mean velocity near the wall is due to the velocity fluctuations and has adverse effects such as increase shear stress on the wall and therefore drag [2].

1.2.5 Normal Reynolds stresses

Figure 1.13 displays the plot of the normal Reynolds stresses for each spatial dimension.

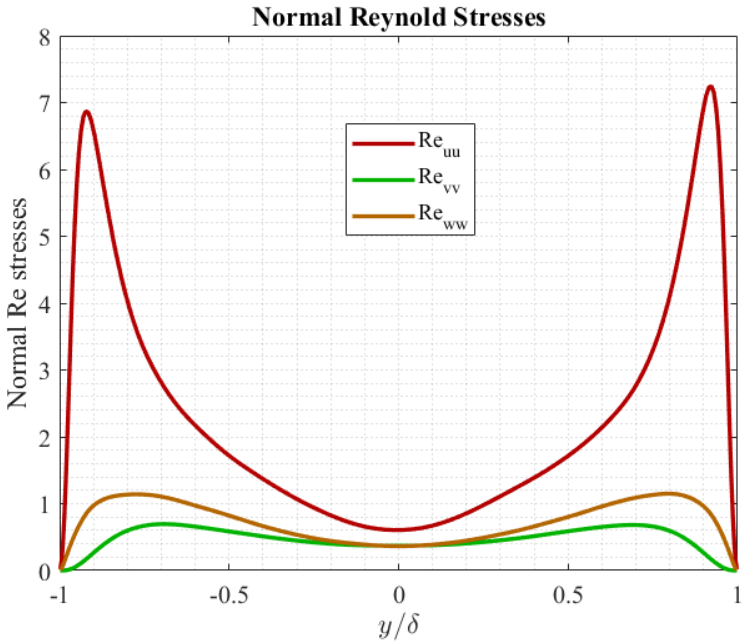

Figure 1.13 – Reynold stresses in the three spatial dimensions.

The Reynolds stresses are the averaged effect of turbulent convection [3] and theoretically should be symmetric with respect to the centreline, however, this is not the case in figure 1.13 as the maximum values of Re_{uu}, for instance, are 6.87 and 7.24 for the left and right peaks respectively. This is due to the lack of statistical convergence. Furthermore, the peaks of the Reynolds stresses should be in conjunction to the peaks of turbulent production, which occur at approximately $y_+ = 10 - 15$ from experimental and numerical results [3] and is where the Reynolds shear stress is equivalent to the viscous stress. To investigate if the results correlate with the results obtained from the assignment, the y_+ value at the maximum Reynolds stress must be determined. This can be executed by first finding the viscous length scale, δ_v, which can be determined from the Reynolds shear number, $Re_\tau = \frac{\delta}{\delta_v}$ (8). Where δ is the channel half height, which is 1 for this instance.

The y_+ value is the ratio of the wall-normal coordinate, y, and the viscous length scale:

$$y_+ = \frac{y}{\delta_v} \tag{9}$$

Executing the above yielded y_+ values of 13.92 for the right and left side peaks in figure 1.13, which correlates with the experimental range of $y_+ = 10 - 15$.

1.2.6 Reynolds shear stress

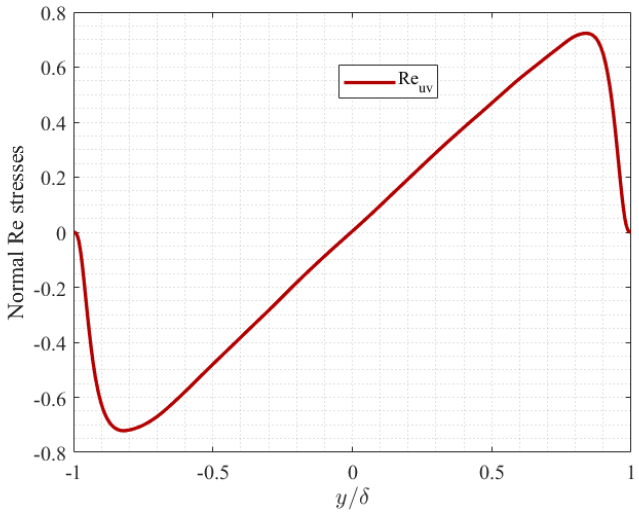

Figure 1.14 – Reynolds shear stress across wall-normal coordinates in the channel.

Figure 1.14 displays the Reynolds shear stress with respect to the wall-normal coordinates. The Reynolds shear stress, $\overline{uv}$, vanishes at the centre line of the channel as the flow is symmetric about this line. Furthermore, it tends to zero due to the no-slip boundary condition present on both walls; where the viscous effects begin to dominate. On a further note, the viscous contribution outside the near wall region is near zero [3], therefore, the Reynolds shear stress is constant until the near-wall region.

The anti-symmetries of the shear layers can be described by considering the flow on either side of the symmetry line, $y/\delta = 0$. To satisfy the symmetry of the flow, the horizontal velocity on the upper and lower half must be equal,

$$u_{upper} = u_{lower} \tag{10}$$

However, the vertical, or wall-normal, must be opposite,

$$v_{upper} = -v_{lower} \tag{11}$$

Therefore, the Reynolds shear stress tends to zero at the centreline and follows an anti-symmetric trend thereon after [3].

Chapter 2

Flow separation in a two-dimensional asymmetric diffuser

2.1 Objectives and overview

The objective of this assignment was to compare the effectiveness of two different turbulence model when simulating a two-dimensional asymmetric diffuser where flow separation is expected to occur due to the adverse pressure gradient caused by the physical geometry. The point of separation, re-attachment and size of recirculation zone is computationally challenging for turbulence models, in which therein lies the reason for this investigation into which predicts these flow characteristics accurately. Establishing the highest accurate model entailed a comparison experimental result are available in papers [5], [6] and [7] , where the velocity profiles, skin friction coefficient and turbulent kinetic energy were to be compared. The $k-\epsilon$ and $k-\omega$ were chosen for the investigation and figure 2.1 displays the asymmetric diffuser with relative dimensions.

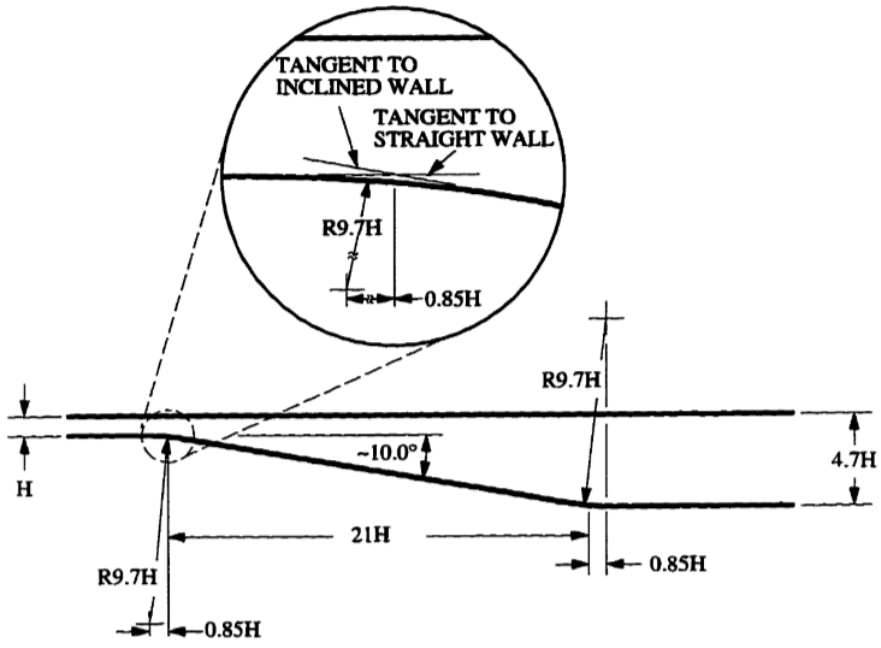

Figure 2.1 – Fluid domain for two-dimensional axisymmetric diffuser, image courtesy of Dr Angela Busse

For this assignment, the streamwise and wall-normal direction are the x and y direction respectively, where the x – axis origin is located at the intersection of the tangents to the straight and inclined walls and the y – axis origin at the same level as the lowest wall. The inlet conditions for the asymmetric diffuser were of a fully developed flow with a Reynolds number, $Re = 20{,}000$, dependent on the centreline velocity, U_c (flow speed at the centreline) and characteristic height, the diameter of the inlet in two-dimensions, of $H = 0.05\ m$.

2.2 Simulating the flow

The commercial Computational Fluid Dynamic software, STAR CCM+, was used to simulate the flow problem. Two simulations were executed in order to simulate the asymmetric diffuser:

(1) The pre-simulation to obtain a data-set of a fully developed velocity profile with its inherent turbulent characteristics. This was executed using a section of the inlet pipe with the use of translational periodic boundary conditions. This type of boundary condition maps the grid fluxes from one boundary to the other in which are commonly referred to as the so-called master and slave boundaries respectively [8]. The flow cycles through the boundaries until a fully developed state, convergence, and was computed for each turbulence model under analysis.

(2) The main simulation was of the asymmetric diffuser with the computed inlet settings and turbulence model. The simulation data was extracted here and compared with the experimental results.

2.2.1 Spatial discretion

STAR CCM+ uses the finite volume method to discretize the fluid domain; this procedure is commonly known as meshing and is where the domain is split into multiple control volumes in which the governing equations of fluid dynamics are solved. These control volumes are more commonly known as cells and the quality of such should be sufficient to not impinge on the numerical solution.

The mesh was provided by Dr Angela Busse and was created using the STAR CCM+ Directed mesher (SDM) in which enables the user to create structured meshes over a fluid continuum [8]. This type of mesh is typically of high-quality as cell defects such as cell skewness, zero volume, or large differentials of volume from cell to cell are avoided. Furthermore, the SDM allows the user to specify the spacing in the near wall regions which entail the height of the first cell next to the wall and the ratio of cell height from the cell layer to the next cell layer. The height of the first cell next to the wall was set such that it correlates with the y_+ value of 1, which places this cell within the viscous sublayer and therefore allows viscous effects to be accounted for which is important when considering flow separation. The ratio of cell layer height was set with hyperbolic spacing where the cell layers closest to the wall transition slower than the cell layers soon after. This produces a highly refined grid in the near wall region. Furthermore, the cells are also characterized with a high aspect ratio as the primary change in flow characteristics is in the wall-normal direction and therefore an aspect ratio of 1 is not required for the full domain. However, a cell aspect ratio of 1 may be useful where the recirculation bubble is expected to appear as the flow can reverse, i.e. change direction, and the high aspect ratio may not capture some of those characteristics.

Figure 2.2 and 2.3 displays the spatial domain of the pre-simulation and main simulation respectively.

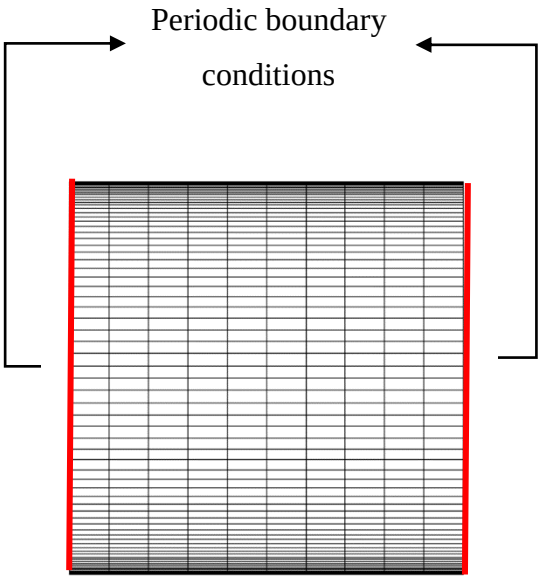

Figure 3.2 – Pre-simulation with translational periodic boundaries highlighted.

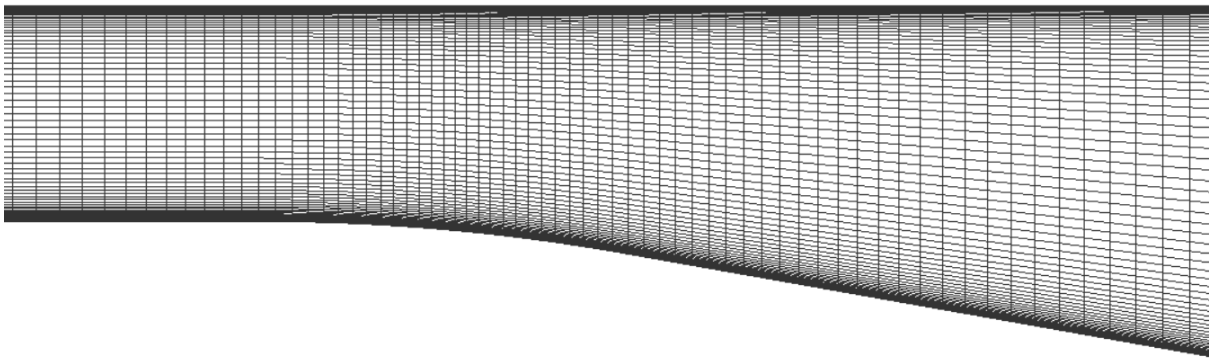

Figure 2.3 – Main simulation, consisting of a structured mesh with hyperbolic spacing at the walls and first near wall cell height with y_+ value selected for 1.

2.3 Discussion on turbulent models

Turbulence models have been in development for decades and are the current solution to the so-called turbulence closure problem where the averaging of the Navier Stokes equations, the statistical equations of turbulence flow, produce more unknown equations within [3]. There have been various types of models in which are displayed in figure 2.4.

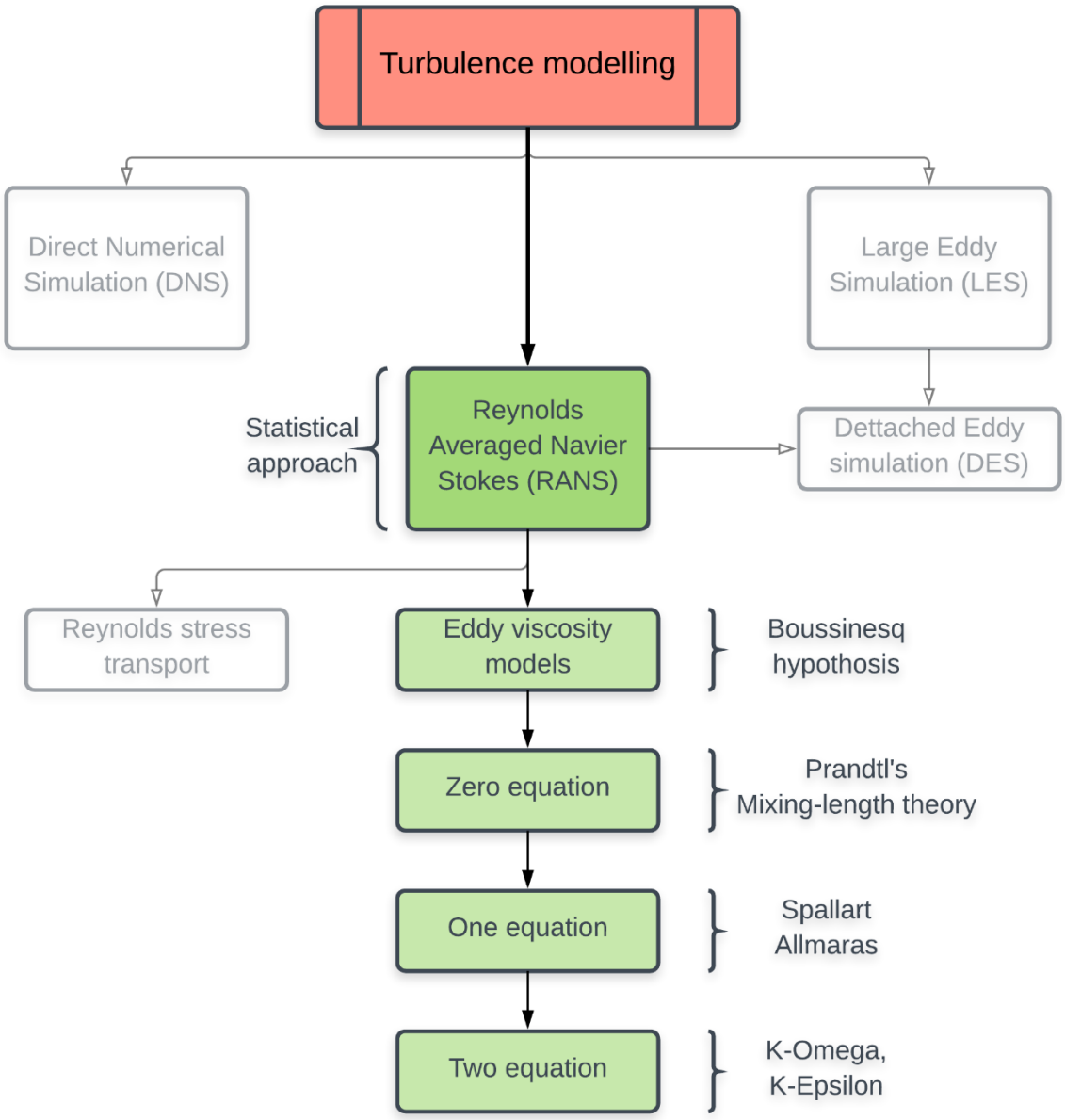

Figure 2.4 – Flow chart detailing turbulence modelling approaches with some examples of the types of Eddy Viscosity models

As previously, averaging the Navier Stokes equations to obtain a statistical description provides a series of unknown equations; 10 equations in total and 6 of which originate from the Reynolds stress tensor [3]. Eddy viscosity models are all based on an assumption that the Reynolds stress tensor is the gradient of the time-mean velocity field, in which is the so-called eddy viscosity [9]. This assignment will focus on the two-equation Eddy Viscosity models; the $k-\epsilon$ and $k-\omega$ models.

Two-equation models are so named as they model the turbulent kinetic energy, k , and another transport equation: the specific dissipation rate of turbulent kinetic energy, ω , for the $k-\omega$ and the dissipation rate of turbulent kinetic energy, ϵ , for the $k-\epsilon$. A priori information on the turbulent structure is not required due to the additional modelling of the turbulent scales through the differential equations predicting the development of the flow of any geometric configuration [3] and therefore two-equation models are considered complete models of turbulent flow [9].

2.3.1 $k-\epsilon$ model

The $k-\epsilon$ model was originally developed by Launder and Jones in 1972 [3] and is widely used in engineering applications. The standard model does not entail wall functions, which was initially problematic as the dissipation of kinetic energy equation contains terms in which cannot be evaluated at the wall [10], therefore, wall functions were required and implemented in later variant models to predict flows in the near-wall region. Furthermore, the model originally poorly predicted flows with strong flow separation and streamline curvature [10] and from this introduced several variations of the model in which the variations that are considered for this assignment are the:

- Low Reynolds, which was proposed by Launder and Sharma and consists of wall and wall damping functions in the near wall region [6] which are used to predict the flow in the boundary.
- v'^2f , which was proposed by Durbin and has seen success in predicting separated flows [6]. This model does not inherently require wall or damping functions that the typical $k-\epsilon$ models requires, but instead, uses differential equations.

2.3.2 $k-\omega$ model

The $k-\omega$ model was originally developed by Willcox in 1993 [3] and consists of a synonymous equation to the $k-\epsilon$ model but in terms of the inverse of the time scale $T=k/\epsilon$, which is equivalent to the specific dissipation of kinetic energy, ω [3]. The model preforms well in the near-wall region without wall functions or wall damping and instead uses easily computed Dirichlet boundary conditions [11]. The model preforms better than its predecessor in adverse pressure gradients, however, exhibits sensitivity to free stream initial conditions

which would significantly affect the final solution. This was rectified with a variation of the model and widely known as the $k-\omega\ SST$, where SST denotes the Shear Stress Transport and was proposed by Mentor in 1993 [3]. This model essentially blends the $k-\omega$ and $k-\epsilon$ in the near-wall and far-field region respectively with the use of blending functions [11] and this improved the models prediction capability in adverse pressure gradients and solved the sensitivity issue to the freestream [3]. With this considered, this assignment will also consider the $k-\omega\ SST$ model for predicting the extent of flow separation in the two-dimensional asymmetric diffuser.

2.4 Results of the turbulence models

In order to produce a Reynolds number of 20,000 based on the centreline velocity, U_c, for each of the models, table 3.1 depicts the required mass flow rates which were set for the periodic boundary.

Table 3.1 – Required mass flow rates with respective models for Re = 20,000

Turbulence model	Mass flow rate, $\dot{m}$ (kg/s)	Centreline velocity, U_c (m/s)
$k-\epsilon$ Low Re	0.3286	6.2665
$k-\epsilon\ v^2f$	0.3279	6.2665
$k-\omega\ SST$	0.3327	6.2746

Evidently from the centreline velocity readings, the $k-\omega\ SST$ model was not able to be precisely calibrated for a Reynolds number of 20,000 despite multiple attempts; this may be due the model still exhibiting slight sensitivity to the freestream, however, an $Re = 20{,}026$ was obtained which is close to the desired Reynolds number.

The velocity magnitude-streamline plots of each of the models is displayed in figures 3.1, 3.2 and 3.3 of the low Re, v^2f and $k-\omega\ SST$ respectively. The markers (black dots) are the starting points of two streamlines which display the extent of the recirculation bubble, if present.

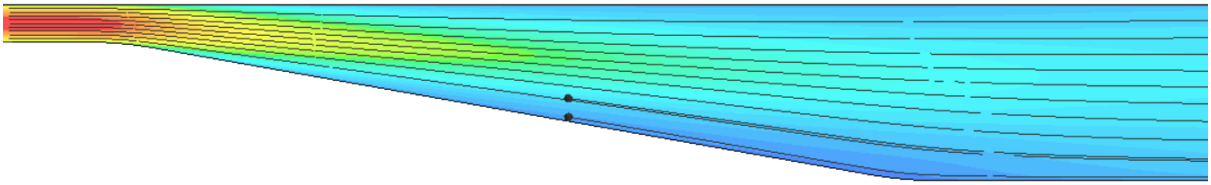

Figure 4.1 – Low Reynolds $k-\epsilon$ velocity - streamline plot.

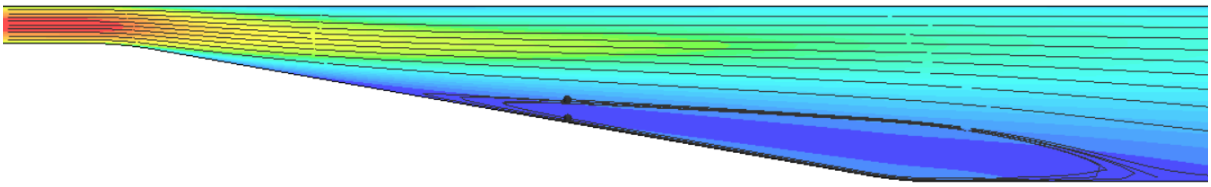

Figure 3.2 – v^2f $k-\epsilon$ velocity-streamline plot

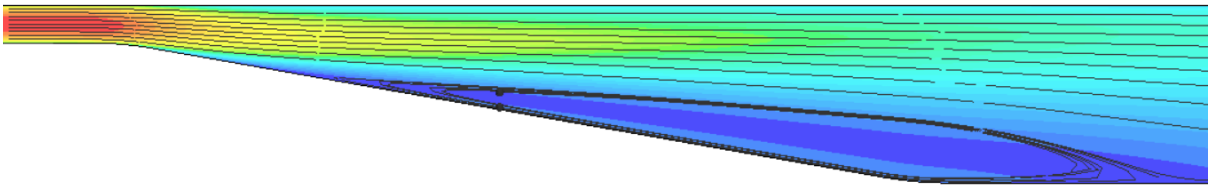

Figure 3.3 – $k-\omega$ SST velocity-streamline plot

From the velocity-streamline plots, clear flow separation can be seen in the diffuser for the $k-\epsilon, v^2f$ and $k-\omega$ SST models, however, the $k-\epsilon$ Low Re does not predict flow separation at all and therefore will not be compared with the experimental results. On an additional note, the separation can be illustrated using a streamwise velocity-contour plot as seen in figure 3.4 for the $k-\omega$ SST, where the negative value of streamwise velocity indicates flow reversal, i.e. flow separation.

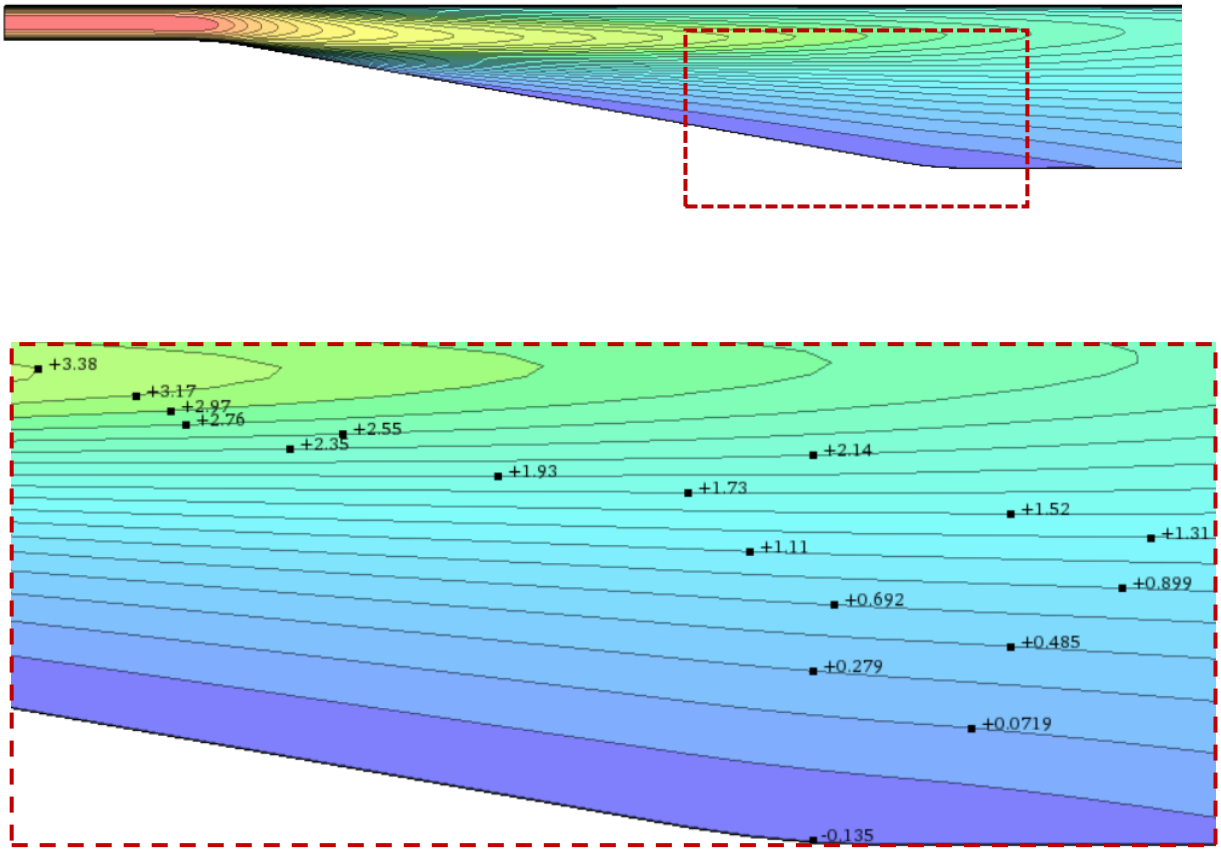

Figure 3.4 – $k-\omega$ SST streamwise velocity contour plot with values indicating velocities. Separation has clearly occurred due to the negative velocity value.

2.4.1 Comparing with experimental results

The velocity profile experimental data was from paper [5] by Buice and Eaton and the simulation results were to be compared at planer sections $x/H = 20.32$ and 46.62; the results were scaled by the bulk velocity, U_b. The skin friction coefficient was from paper [6] by Laccarino and was to be compared on the lower wall of the diffuser, note, no scaling is used as the coefficient of friction is already non-dimensional. Lastly, the turbulence kinetic energy was from the paper [7] by Obi and was compared at $x/H = 19.2$, where the scaling was the centreline velocity squared, U_c^2.

The skin friction coefficient is a useful parameter to establish the extent of flow separation as the coefficient of friction becomes negative due to the flow reversal. However, STAR CCM+ takes the modulus of the wall-shear stress [12] which results in a constant positive sign and therefore post-processing of the data was required. The flow separation and re-attachment point was deemed when the skin friction coefficient intersected with the x – axis and changed direction [12] and a simply procedure was required to invert the sign in between these points. Figure 3.5 displays the post-processed coefficient of friction of the turbulence models compared with the experimental results.

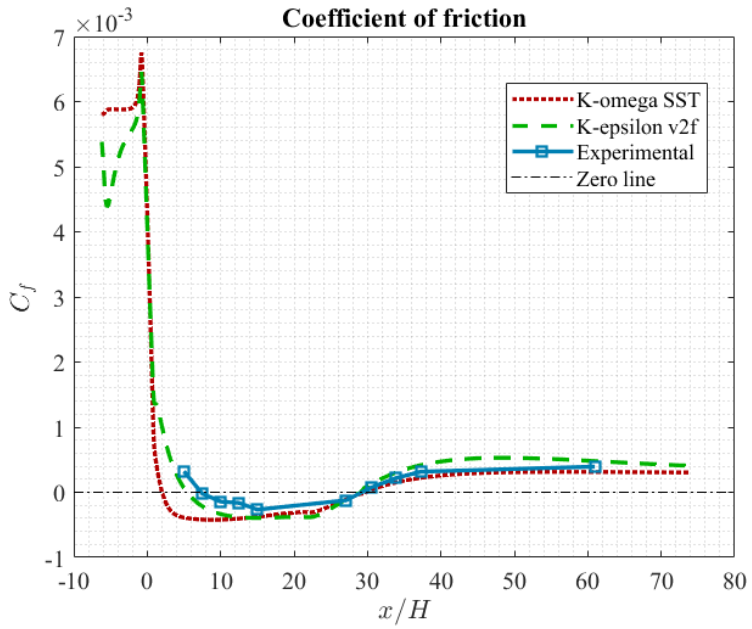

Figure 3.5 – Coefficient of friction of the $k-\epsilon$, $k-\omega$ in comparison with the experimental results of [6]

The separation points and re-attachment points are displayed in table 3.1 below:

Table 3.1 – Separation and re-attachment points in x/H

	Separation	Re-attachment
Experimental	7.2	29.25
$k-\epsilon\ v^2f$	5.5	29.1
$k-\omega\ SST$	2	29.8

From the results, the $k-\epsilon\, v^2 f$ clearly predicts the separation and re-attachment points more accurately than its counterpart, however, slight variations from the experimental values are present.

The velocity profiles for $x/H = 20.32$ and 46.62 are displayed in figures 3.6 and 3.7 respectively.

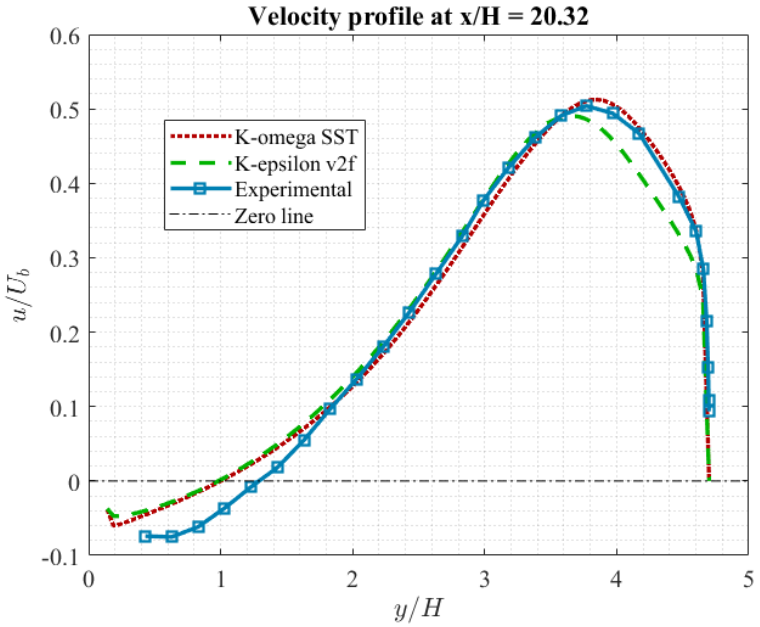

Figure 3.6 – Velocity profile at x/H = 20.32, normalized by the bulk velocity and in comparison with experimental results from [5]

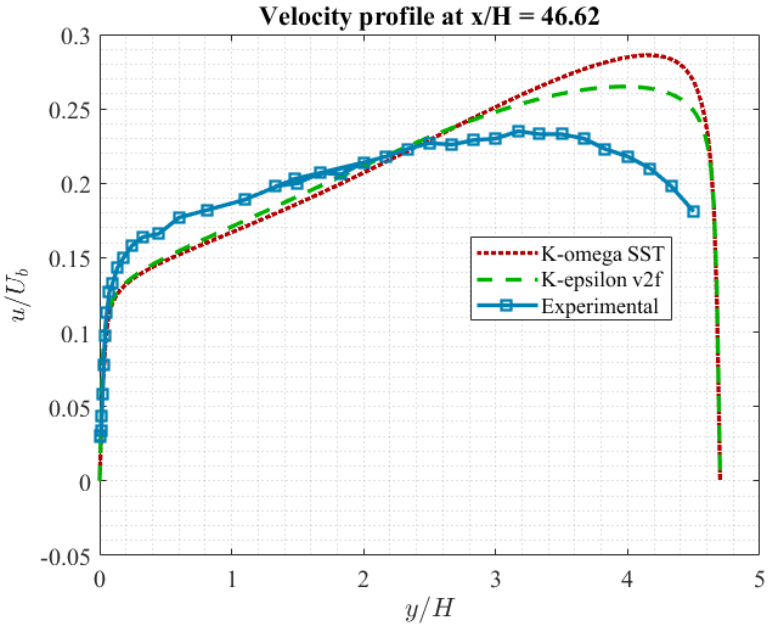

Figure 3.7 – Velocity profile at x/H = 46.62, normalized by the bulk velocity and in comparison with experimental results from [5]

The turbulence models significantly under predict the recirculation velocity in the streamwise direction as seen in figure 3.6. The development of the flow downstream of the re-attachment point is clearly not accurately captured, however, this may be due to the non-homogenous spatial nature of flow separation in all three dimensions [6], and the two-dimensional simulation does not account for one of these dimensions despite the diffuser being asymmetric.

The turbulence kinetic energy at $x/H = 19.2$ is displayed in figure 3.8 below:

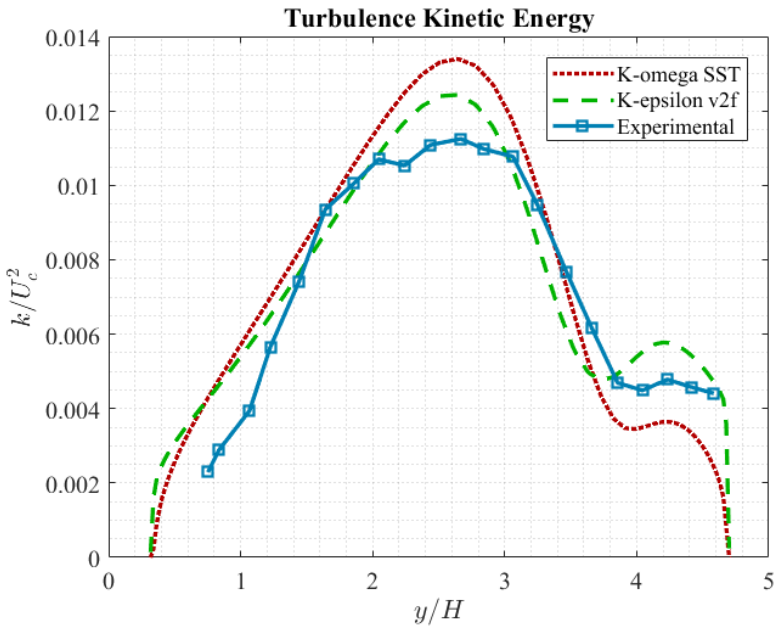

Figure 3.8 – Turbulence kinetic energy comparison at x/H = 19.2, normalized by the centreline velocity squared and in comparison with experimental results from [7]

x/H of 19.2 is within the vicinity of the separation bubble and according to figure 3.6, this bubble is approximately from $y/H = 1 - 1.2$ with respect to the wall-normal direction. Both turbulence models significantly overpredict the turbulence kinetic energy in the separate region; at $y/H = 0.65$, the overpredicted is by approximately 110% (210% in total) for both models. However, the accuracy of both turbulence models improves, with the exception at the channel centreline, and the $k - \omega$ being slightly superior.

2.4.2 Conclusion

With regards to the point of separation and re-attachment, the $k-\epsilon\ v^2f$ model produced more accurate results than the $k-\omega\ SST$ model for the two-dimensional asymmetric diffuser, however, both failed to accurately predict the development of the flow after the re-attachment point. This may be due to the non-homogenous spatial nature of flow separation in all three dimensions, and the two-dimensional simulation does not account for one of these dimensions despite the diffuser being asymmetric. The $k-\omega$ predicts the velocity profiles and turbulence kinetic energy slightly better than the $k-\epsilon\ v^2f$.

With all considered, both models have strong and weak points, however, some of the weak points may be due to the two-dimension approach of the simulation. As a recommendation, the $k-\epsilon\ v^2f$ model should be used for the prediction of the flow separation point and re-attachment, however, this recommendation may change if the simulation was conducted in three-dimensions instead of two.

3. References

[1] J. L. **Aragon**, G. Naumis, M. Bai, M. Torres and P. Maini, "Turbulent luminance in impassioned van Gogh paintings," physics.fluid-dyn, 2006.

[2] D. A. Busse, "Turbulent Flow lecture notes, Chapter 1," pp. 9,10, 2018.

[3] P. A. Durbin and B. A. P. Reif, Statistical Theory and Modeling of Turbulent flows, Chichster: John Wiley & Sons, 2011, pp. 1-60.

[4] D. A. Busse, "Turbulent flow lecture notes, Chapter 3," 2018.

[5] C. U. Buice and J. K. Eaton, "Experimental investigation of flow through an asymmetric plane diffuser," Standford University, Stanford, USA, 1997.

[6] G. Laccarino, "Predictions of a turbulent seperated flow using commercial CFD codes," *Journal of Fluids Engineering,* vol. 123, no. 819, pp. 819-828, 2001.

[7] O. Shinnosuke, K. Aoki and M. S., "Experimental and Computational study of turbulent seperating flow in an asymmetric plane diffuser," in *Turbulent shear flows,* Kyoto, Japan, 1993.

[8] C. A. STAR CCM+, "STAR CCM+ User guide," CD ADAPCO.

[9] C. Belloni, "Hydrodynamics of Ducted and Open-Centre Tidal Turbines," University of Oxford, Oxford, 2013.

[10] Fluent ANSYS, "Modeling turbulent flows," 2006. [Online]. Available: http://www.southampton.ac.uk/~nwb/lectures/GoodPracticeCFD/Articles/Turbulence_Notes_Fluent-v6.3.06.pdf. [Accessed 13 4 2018].

[11] F. R. Menter, "Zonal two equation k-w turbulence models for aerodynamic flows," in *24th Fluid Dynamics Conference,* Orlando, Florida, 1993.

[12] A. Busse, "Flow in an asymmetric diffuser - 2nd lab hand out," University of glasgow, Glasgow, 2018.

[13] V. V. Gogh, Artist, *Starry night.* [Art]. 1889.

[14] M. o. M. Art, “momo,” [Online]. Available: https://www.moma.org/collection/works/79802?artist_id=2206&locale=en&page=1&sov_referrer=artist. [Accessed 14 4 2018].